James Madison University

JMU Scholarly Commons

Senior Honors Projects, 2020-current | Honors College

5-8-2020

Curvature in compressed thin cylindrical shells approaching the isometric limit

Nicole Voce

Follow this and additional works at: https://commons.lib.jmu.edu/honors202029

 Part of the Condensed Matter Physics Commons

Recommended Citation

Voce, Nicole, "Curvature in compressed thin cylindrical shells approaching the isometric limit" (2020). *Senior Honors Projects, 2020-current*. 45.
https://commons.lib.jmu.edu/honors202029/45

This Thesis is brought to you for free and open access by the Honors College at JMU Scholarly Commons. It has been accepted for inclusion in Senior Honors Projects, 2020-current by an authorized administrator of JMU Scholarly Commons. For more information, please contact dc_admin@jmu.edu.

Accepted by the faculty of the Department of Physics and Astronomy, James Madison University, in partial fulfillment of the requirements for the Degree of Bachelor of Science.

FACULTY COMMITTEE:

Dr. Klebert Feitosa
Associate Professor, Department of Physics and Astronomy, James Madison University

---

Dr. Marcelo Dias
Assistant Professor, Department of Engineering, Aarhus University

---

Dr. Kendra Letchworth-Weaver
Assistant Professor, Department of Physics and Astronomy, James Madison University

---

Dr. Bradley R. Newcomer
Honors College Dean

Curvature in Compressed Thin Cylindrical Shells Approaching the Isometric Limit

---

A Project

Presented to

the faculty of the Undergraduate College of

Science and Mathematics

James Madison University

In Partial Fulfillment

of the Requirements for the Degree

Bachelor of Science

---

by

Nicole Voce

2020

© Copyright by Nicole Voce 2020

All Rights Reserved

I dedicate this thesis to my parents.

Thank you for always believing in me.

Contents

List of Tables

List of Figures

Acknowledgments

I would like to thank Drs. Dias and Feitosa for always supporting me over the course of this research project. I would not have been able to complete it if it were not for their endless encouragement and dedication to their research and students. I would also like to thank Luis De Cunto for his invaluable work developing the numerical simulations and Cassidy Anderson for constructing the origami representation of the Yoshimura pattern.

Abstract

The ability to manipulate surface elastic instabilities finds many applications in engineering smart interfaces, e.g. in fluid-structure interaction and micro-fabrication. We study the buckling of a thin cylindrical shell constrained to slide onto an inner non-deformable pipe. Our goal is to characterize the relationship between the shell thickness and the localization of stresses by using curvature measurements. First, we induce surface buckling by immobilizing one end of the shell and applying force to the other end. Then, we obtain a virtual reconstruction of the surface from 3D optical scanning and compute the Gaussian curvature for every point on the mesh. We find that as the shell gets thinner, the distribution of Gaussian curvatures becomes broader. Furthermore, measurements of areas enclosed by the parabolic lines around protruding vertices from the buckled surface show that the transitions between regions of positive and negative curvature are more localized. Finally, the Gaussian curvature reveals the formation of substructures within the lobes around the vertices. The localization results demonstrate that the cylindrical shell clearly evolves towards the isometric limit represented by the well-known Yoshimura pattern. However, the emergence of substructures indicates that this evolution is more complex than originally anticipated.

1 Introduction

To most, the word "buckling" invokes images of an object being compressed to the point of potentially catastrophic failure. Indeed, there are instances where buckling causes extensive damage to large, important structures that we rely on. It is not uncommon for a silo or large tank to buckle, causing the entire structure to collapse [1]. In 1963, the Atlas Agena D rocket depressurized on its launch pad, causing the upper stage to buckle which resulted in the entire rocket collapsing in half [12]. Buckling, specifically the buckling of cylindrical shells such as silos, tanks, and rockets, has long been the adversary of many engineers. Traditional approaches to the study of shell buckling have mainly focused on determining the first or second buckling loads and the initial post-buckling equilibrium paths in order to prevent ultimate failure [1]. However, there has been a paradigm shift in thin shell mechanics. Up until recently, shell buckling was viewed as a catastrophic failure that was to be prevented. Now, the dynamics behind shell buckling are being exploited to advance shape-changing technologies. These 'morphing' structures find applications in haptic electronic displays and aerodynamical surfaces that can change from being smooth to rough and back again [2], [3]. The push towards using these failure modes advantageously has opened a floodgate of questions ranging from how to control the dynamics of shell buckling to more fundamental ones about how the actual buckling pattern is formed.

In general, the walls of thin shells have membrane stiffness several orders of magnitude greater than the bending stiffness. To deform a thin shell, it must absorb as much bending strain energy as membrane strain energy. If most of this strain energy is in the form of membrane compression, and if this membrane energy can be converted into bending energy, the shell may experience buckling [1]. The way the shell buckles depends on multiple factors, including how the shell is loaded, boundary con-

ditions, and its geometrical and material properties. Buckling behavior is also heavily influenced by the structure's maximum load sensitivity to initial imperfections. In the case of cylindrical shells, this imperfection sensitivity has lead to the increasing discrepancy between test and theory with increasing radius-to-thickness ratio [13]. The Koiter theory [14] provides a rigorous proof of the critical axial load's extreme sensitivity to initial geometric imperfections. Due to the disconnect between test and theory, it is hard to predict how a cylindrical shell will buckle. However, by internally constraining a thin cylindrical shell with a rigid body, one can force the majority of the deformation and energy into localized peaks. The addition of an internal support introduces some degree of control over the surface pattern produced by buckling. In order to successfully utilize this post-buckling pattern in tunable surfaces, we must understand what factors influence its appearance. Namely, we look to explain how the surface stresses distribute as a function of shell thickness.

(a) Origami representation of the Yoshimura pattern.

(b) Experimental apparatus with 50.8 μm shell.

Figure 1.1: Origami shell and experimental shell.

In order to understand the stress distribution on a constrained thin cylindrical

shell, we first consider the case of an unconstrained thin cylindrical shell experiencing compression. The thin shell buckles in a seemingly random way and a pattern emerges that appears similar to the pattern on a thin sheet after it has been crumpled and then flattened. In our work, we construct thin cylindrical shells from thin sheets; thus, we look at the stress localization of crumpled thin sheets in order to gain intuition on how thin cylinders deform as they evolve towards the isometric limit. Isometric deformations are those in which stretching is zero. We expect the isometric limit to be represented by the well-known Yoshimura pattern (Fig. 1.1a); the post-buckling pattern is expected to evolve towards the origami Yoshimura pattern as the shell thickness decreases due to the thickness-dependence of bending and stretching energies.

When thin sheets are crumpled, line-like ridges and point-like peaks appear on their surfaces [4]. Although the produced pattern is seemingly random and uncontrollable, elasticity and confinement force the sheet to favor isometric deformations by stacking layers of material without focusing [15]. We can understand the role stretching plays in this deformation by first looking at an isolated fold where a sheet is bent around an undetermined radius of curvature. As this radius of curvature decreases, the fold will appear sharper, due to the fact that bending energy is proportional to the curvature square of the fold. However, the sheet cannot allow the radius of curvature to become infinitely small so it must find a better energy balance by concentrating stretching into a very localized region along the entire fold.

The simplest way to model stress localization in thin sheets is the d-cone, also referred to as the 'developable' cone. Consider a flat disk that rests concentrically on a simple rim. When a point force is applied to the center of the disk, the disk experiences an increasing amount of in-plane circumferential compression that cannot be maintained indefinitely. As a result, part of the disk buckles upwards and separates

from the rim, relieving the system from the compression. The resulting shape is the d-cone mode shape [5].

One can study the d-cone in two different forms: continuous and discrete. The continuous d-cone is created using the aforementioned method whereas the discrete d-cone is created using a pre-folded disk. Folding the disk allows continuous motion up to a point where all facets can "flat-fold" and contact each other in a vertical plane under fold rotations equal to 180° [5]. Like the discrete d-cone, the Yoshimura pattern is also flat-foldable. If we connect multiple discrete d-cones together in a cylindrical shape, we can recover the Yoshimura pattern (Fig. 1.1a).

By viewing the Yoshimura pattern in this perspective, the standard single d-cone calculations can be expanded upon and adapted for this larger system. In particular, the amount of out-of-plane angular deflection for a single d-cone is calculated using the Gauss mapping technique by considering the deformed shape in terms of normal vectors to the surface of the disk [5]. By considering the Yoshimura pattern in terms of discrete d-cones, that calculation can be applied directly to this more robust structure: the amount of out-of-plane angular deflection for the Yoshimura pattern can be calculated using the same Gauss mapping technique. Gauss's theorem states that the area of the Gauss map is equal to the angular deficit at the vertex and that the angular deficit produces Gaussian curvature [6]. Gaussian curvature is the product of the two principal curvatures and its presence necessarily produces a strain field [7]. Thus, the amount of Gaussian curvature is indicative of how much stretching energy is contained within the surface. In order to understand how the thickness of a sheet affects stress localization, we must first derive the total elastic energy equation of thin sheets.

1.1 Theory of Shell Mechanics

Detailed explanations and analysis of thin shell theory can be found in standard texts [16-19]. Here, we present an abridged version of the derivation of the total elastic energy equation of thin sheets from [8]. We begin this derivation by first defining the geometrical quantities necessary to describe curved surfaces and their deformations. Then, we establish the surface's metric properties, namely the local measure of distances between material points, as well as the measure of curvature that quantifies warping and bending of the surface. From these, we define in-plane strain and curvature strain. Finally, we construct the total elastic strain energy equation.

Derivation of Elastic Energy

Consider an undeformed shell with a collection of mid-surface material points, call this collection $\overline{S}$. We can map $\overline{S}$ in 3D Euclidean space by a three component vector function $\mathbf{S}:\overline{S} \to \mathbb{R}^3$, where $\mathbf{S}(x^1, x^2) = (S_1(x^1, x^2), S_2(x^1, x^2), S_3(x^1, x^2))$ and (x^1, x^2) are the local Lagrangian coordinates on $\overline{S}$. We then calculate the induced prescribed metric–a function that defines a distance between each pair of elements of a set– for $\overline{S}$ to be $\bar{\mathbf{a}} = (\partial_\alpha \mathbf{S} \cdot \partial_\beta \mathbf{S})\mathbf{dx}^\alpha \otimes \mathbf{dx}^\beta$. Now consider a deformed shell with a collection of mid-surface material points, called S. We can construct a deformation map $\mathbf{F}:\overline{S} \to S$ which will induce a target metric represented by $\mathbf{a} = (\partial_\alpha \mathbf{F} \cdot \partial_\beta \mathbf{F})\mathbf{dx}^\alpha \otimes \mathbf{dx}^\beta$. From here, we see that the reference and target components of the metric tensor, called the first fundamental form, are given by

$$\bar{a}_{\alpha\beta} = (\partial_\alpha S \cdot \partial_\beta S) \tag{1.1}$$

$$a_{\alpha\beta} = (\partial_\alpha F \cdot \partial_\beta F). \tag{1.2}$$

(1.1) and (1.2) establish local measures of distances between material points. We can define the unit normals to the reference surface $\bar{S}$ and the target surface S by $\bar{\mathbf{N}} = (det\ \bar{\mathbf{a}})^{-\frac{1}{2}}\ \partial_{\mathbf{1}}\mathbf{S} \times \partial_{\mathbf{2}}\mathbf{S}$ and $\mathbf{N} = (det\ \bar{\mathbf{a}})^{-\frac{1}{2}}\ \partial_{\mathbf{1}}\mathbf{F} \times \partial_{\mathbf{2}}\mathbf{F}$, respectively. We can recover the reference and target components of the curvature tensor, otherwise known as the second fundamental form, by taking the second derivative of the mapping of the material points of both $\bar{S}$ and S and projecting them onto the direction of their respective normal fields. These components are

$$\bar{b}_{\alpha\beta} = \bar{\mathbf{N}} \cdot \partial_\alpha \partial_\beta \mathbf{S} \tag{1.3}$$

$$b_{\alpha\beta} = \mathbf{N} \cdot \partial_\alpha \partial_\beta \mathbf{F}. \tag{1.4}$$

The matrices $\overline{\mathbf{a}}^{(-1)}\overline{\mathbf{b}}$ and $\mathbf{a}^{-1}\mathbf{b}$ are the shape operators on the reference and target shells respectively. Their eigenvalues are the corresponding principal curvatures.

We define the pure in-plane displacement as $u^\alpha(x^1, x^2)$ and the out-of-plane displacement as $v(x^1, x^2)$ in our displacement field. The complete deformation of the mid-surface of the shell is given by the function $\mathbf{F} = \mathbf{S} + \mathbf{U}$ where $\mathbf{U}(\mathbf{x^1}, \mathbf{x^2}) = \mathbf{u}^\alpha(\mathbf{x^1}, \mathbf{x^2})\partial_\alpha \mathbf{S} + \mathbf{v}(\mathbf{x^1}, \mathbf{x^2})\bar{\mathbf{N}}$ is the displacement vector in normal coordinates. Now we define the in-plane strain, $\epsilon_{\alpha\beta}$, as a measure of stretching and the curvature strain, $\kappa_{\alpha\beta}$, as a measure of bending.

$$\epsilon_{\alpha\beta} = \frac{1}{2}(a_{\alpha\beta} - \bar{a}_{\alpha\beta}) \tag{1.5}$$

$$\kappa_{\alpha\beta} = (b_{\alpha\beta} - \bar{b}_{\alpha\beta}) \tag{1.6}$$

We can now write the total elastic energy as a surface integral of energy density as follows:

$$\varepsilon = \frac{Et}{2(1-v^2)} \int dA[(1-\nu)\mathrm{Tr}(\epsilon^2) + \nu(\mathrm{Tr}(\epsilon))^2 + \frac{t^2}{12}((1-\nu)\mathrm{Tr}(\kappa^2) + \nu(\mathrm{Tr}(\kappa))^2)] \tag{1.7}$$

where E is the Young's Modulus, ν the Poisson ratio, and t is the thickness of the shell. It is important to note that the trace operation, Tr, on any matrix $\mathbf{M}$ is taken in a specific way that depends on the metric of the reference state in the following way: $\mathrm{Tr}(\mathbf{M}) \equiv \bar{\mathbf{a}}^{\alpha\beta} M_{\alpha\beta}$. In equation 1.7, the terms proportional to t compose the stretching energy while the terms proportional to t^3 compose the bending energy.

From equation 1.7, thickness-dependent balance equations can be derived. These balance equations establish the presence of a boundary layer. Bending with stretching happens within the boundary layer while pure bending occurs outside of it [8]. We can understand how stretching localizes in the boundary layer by solving one of the balance equations; the solution is given by a stress potential in which its source is the Gaussian curvature.

In this thesis, we explain the mechanics behind the buckling of internally constrained, monocoque cylinders (Fig. 1.1b) by investigating the influence of shell thickness on the localization of surface stresses through curvature analysis. We focus on the geometric features of the buckled pattern to make a connection between the emerging pattern on shells of finite thickness and the isometric limit, represented by the Yoshimura pattern. This thesis expands upon the work done on the axial-buckling of thin-walled cylinders by Seffen and Stott [9]. Using an updated version of the experiment described by Horton and Durham [20], they showed that the size of the buckles depends only on the cylindrical radius and gap width and not on the thickness of the shell.

We are interested in characterizing the buckled pattern of internally constrained, monocoque cylinders in terms of thickness-dependence for tunable surface applications. Emerging controllable surface technologies have applications in areas such as aerodynamics and hydrodynamics: by allowing the surface to switch from being

smooth to rough, and back again, the fluid flow can be disrupted, thus altering the drag experienced. Due to the uniformity of the buckled pattern and the ease at which it can be produced, a constrained thin cylindrical shell provides an ideal basis to study controllable surfaces. Therefore, we propose a systematic study of the dependence of the localization of surface stresses on shell thickness to build a deeper understanding of deformations experienced by internally constrained monocoque cylinders.

2 Experimental Methods

In this chapter, we describe the methodologies developed to construct internally constrained monocoque cylinders and the Yoshimura pattern.

2.1 The compressed cylindrical shell

The shells we use in the experiment are made of thin Mylar sheets, a polyester film made from stretched polyethylene terephthalate (PET) suitable for our the experiment because of its high tensile strength and its resistance to fractures and tears. Mylar is commercially available in transparent, semi-clear white or reflective silver surface from suppliers such as McMaster Carr (mcmaster.com) and SPI Supplies (2spi.com) in thicknesses ranging from 0.254 mm to 0.0025 mm. It has a Young's modulus of 2-2.7 GPa and a Poisson ratio of 0.38 before yield and 0.58 after yield. Eight different Mylar thicknesses were used to construct the cylindrical shells whose properties are listed in Table 2.1.

Thickness (μm)	Diameter $\pm$ 0.05 (mm)	Gap Distance $\pm$ 0.035 (mm)	Height $\pm$ 0.5 (mm)
178 $\pm$ 18	15.804	0.564	157
127 $\pm$ 13	15.88	0.640	157
102 $\pm$ 10	16.336	1.096	158
76 $\pm$ 7.6	16.172	0.932	158
51 $\pm$ 5.1	16.275	1.035	157.5
25 $\pm$ 2.5	16.495	1.255	158
6.0 $\pm$ 0.1	16.102	0.862	59.6
2.5 $\pm$ 0.1	17.249	2.009	62.3

Table 2.1: Table of experimental parameters for each shell thickness.

The shell is assembled as follows. First, we cut a rectangular piece of Mylar of dimensions 15.75 cm x 22 cm (0.052 mm thickness and above) or 6 cm x 22 cm (0.0060 and 0.0025 mm thicknesses) using a laser cutter (ULS Versa Laser VLS 3.50 with a 50W laser). To help avoid immediate edge collapse, two thicker strips of Mylar (0.178

mm) are adhered to the longer edges of the Mylar rectangular sheet using double sided stick Scotch Tape. Then, the reinforced rectangle is next wrapped around a PVC tube of diameter of $d_0 = 60 \pm 6$ mm. Seffen and Stott [9] have found that the pattern that forms on the thin cylindrical shell under compression depends on the gap between the Mylar and the tube. To control the gap size, we have used the same technique reported in [9] of inserting a rodlike shim ($\frac{1}{16}$ in. stainless steel rod, annealed) between the sheet and the tube before connecting the edges of the sheet in a narrow overlapping seam with Scotch Tape. Once the Mylar is tightly wrapped around the tube, the shim is removed and the excess Mylar trimmed. Despite rigorously following the same procedure for all shells, small variations in the overlap seam (which are difficult to control experimentally) result in significant variation in the gap from shell to shell. We determined the gap by measuring the perimeter p of each shell and computing $(p/\pi) - d_0$. The result is found in Table 2.1.

Once the cylindrical shells were assembled, we applied a thin uniform coat of white acrylic paint to the outer surface (Master Airbrush Cool Runner II Airbrushing System). This step is necessary because the scanner cannot capture the features of reflective surfaces.

To uniformly buckle the cylinder, plastic braces were fashioned to fit snugly around the PVC tube, resting just above the Mylar. The top brace is then compressed, forcing the Mylar to buckle. Once a uniform pattern is achieved, the top brace is secured with a screw, ensuring that the Mylar stays in its buckled state for scanning. Figure 1.1b shows a compressed shell ready for scanning.

2.2 Scanning the surface

This study focuses on the nature of the buckling pattern of the compressed thin cylinder. It is performed on 3D meshes generated for each shell with an EinScan Pro scanner. This scanner is able to resolve features as small as 0.05 mm on the surface.

We set the compressed shell on the instrument turntable and performed fixed auto 3D scans of the surfaces by taking snapshots every 7 degrees (50 steps over a 360 degree scan). After the scan was complete, we create an *unwatertight* model in the scanner's software. To create an unwatertight model, the software uses an algorithm to mesh the point cloud such that it only connects points within a certain distance without filling holes. After the unwatertight model is created, we use the software to fill any holes with a perimeter greater than 10 mm. We then use the scanner's smoothing function to improve data quality. The output file is then saved in stereolithographic format (.stl) for further processing and analysis.

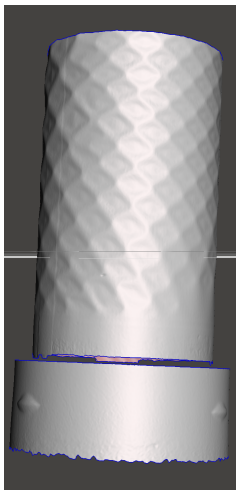

Figure 2.1: 3D reconstruction of point-cloud mesh outputted by 3D scanner.

The complete scan includes not only the Mylar shell, but also sections of the the plastic braces as shown in figure 2.1. We import the mesh into MeshMixer (meshmixer.com) to crop and align the mesh. Figure 2.2 shows all shells considered in this study, labeled by their respective thickness. Subsequently, we obtain detailed views of the protruding vertices, illustrated in figure 2.3, by cropping the cylindrical shells in MeshLab (meshlab.net). After all crops are completed, we process the mesh further.

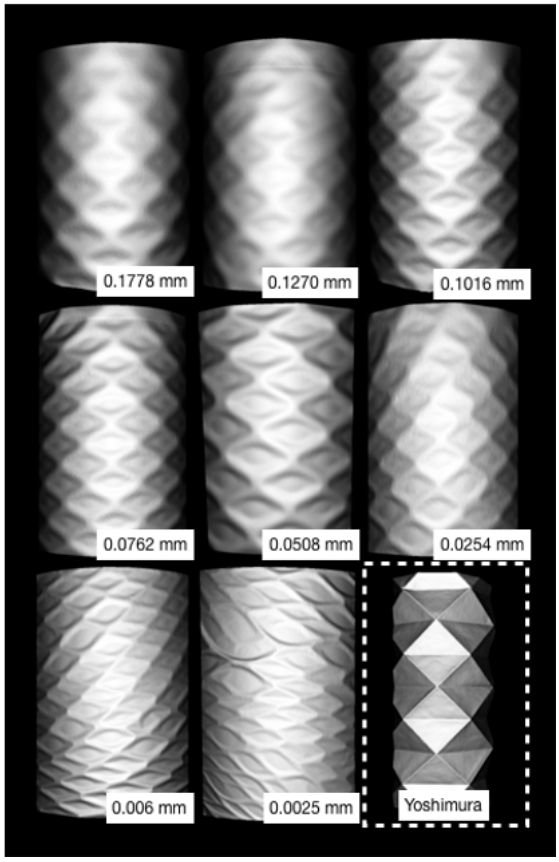

Figure 2.2: 3D scanned images of experimental model with eight different shell thicknesses.

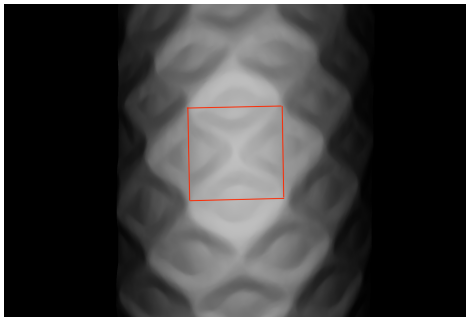

Figure 2.3: 3D reconstruction of scanned cylinder. Red lines indicate path of crop.

2.3 Yoshimura origami construction

As discussed in the introduction, the stretching energy becomes increasing costly for ever thinner shells. Consequently, we expect the features of the buckled pattern

to become more localized as the shell approaches the isometric limit. At this limit the buckling pattern resembles the Yoshimura pattern, which allows a cylindrical shell to buckle without stretching. To compare the evolution of the thin Mylar shell with the Yoshimura pattern, we constructed an origami representation of the Yoshimura pattern by making a grid of $1\ in. \times 1\ in.$ angled squares with horizontal lines through their centers on origami paper (Folia Paper, Transparentpapier, 42 g/m^2) in Inkscape. We then perforated the lines using a laser cutter and folded along those lines to reconstruct a cylindrical Yoshimura pattern as shown in figure 1.1a. The Yoshimura pattern was then scanned and the point cloud processed for further analysis.

Once we have our face and vertices cropped, we apply smoothing steps to reduce the noise from the scanner. Then, we compute the mean and Gaussian curvatures of both the face and the vertices in MATLAB. This will be the topic of the next chapter.

3 Computing Curvatures

In this chapter, we discuss the MATLAB code used to calculate the mean and Gaussian curvatures of our buckled surfaces as well as the techniques used to process the meshes.

3.1 Curvature Code

We computed the mean and Gaussian curvatures of our buckled shells in MATLAB using a code that had been previously developed by Mark Meyer *et. al* [10]. This method utilizes triangular meshes, as it is often considered the most reliable approximation of continuous surfaces. The geometric quantities of the surface are defined at each vertex as spatial averages around the vertex. If these averages are made consistently, the geometric property at a given vertex will converge to the pointwise definition as local sampling increases, allowing the definitions of curvature or normal vector to extend from the continuous case to discrete meshes. The spatial averages are restricted to be within the immediate neighboring triangles, an area which Meyer *et. al* refers to as the 1-ring neighborhood. The averaging area is restricted to a family of special local surface patches that are contained within the 1-ring neighborhood of each vertex with piecewise linear boundaries crossing the mesh edges at their midpoints. A precise surface patch that optimizes the accuracy of our curvature operators is then found. We now discuss the derivation of the discrete mean curvature normal operator and the discrete Gaussian curvature operator as developed and explained by Meyer *et. al* in their paper.

Discrete Mean Curvature Operator

In order to compute the discrete mean curvature operator (and thus the mean curvature), Meyer *et. al* first derive the local integral using finite volume. A linear

interpolation between the three vertices of a triangle is selected and for each vertex, an associated surface patch (a finite volume) over which the average will be computed, is chosen. The piecewise linear boundaries of the surface patch connect the midpoints of the edges emanating from the center vertex and a point within each adjacent triangle. This area is what they computed the integral of the mean curvature over.

The mean curvature normal operator is a generalization of the Laplacian from flat spaces to manifolds. Gauss's theorem says that the integral of the Laplacian over a surface going through the midpoint of each 1-ring edge of a triangulated domain can be expressed as a function of the node values and the angles of the triangulation. Thus, they achieved a general formula that is valid for any triangulation

$$\int\int_{\mathcal{A}_{\mathcal{M}}} \mathbf{K}(\mathbf{x})\, dA = \nabla A_{1-ring}$$

where $\mathbf{K}(\mathbf{x})$ is the mean curvature normal operator A_{1-ring} is the surface area for the entire 1-ring neighborhood. In order to provide an accurate estimate of the spatial average, they must chose one finite volume region. They chose the Voronoi region of each sample because, by definition, it minimizes the discrepancy between the local spatial average of the mean curvature with the actual pointwise value. They use the vertices of the mesh as sample points and pick the Voronoi cells of the vertices as associated finite-volume regions. However, the Voronoi region is inaccurate for obtuse triangles. Thus, they define a mixed area, A_{mixed}, as follows: for non-obtuse triangles, the circumcenter point is used, and for obtuse triangles, the midpoint of the edge opposite to the obtuse angle is used to construct our new surface area. Now that the mixed area is defined, they can express the mean curvature normal operator

as

$$\mathbf{K}(\mathbf{x}_i) = \frac{1}{2A_{mixed}} \sum_{j \in N_1(i)} (\cot \alpha_j + \cot \beta_j)(\mathbf{x}_j - \mathbf{x}_i) \tag{3.1}$$

where α_{ij} and β_{ij} are the two angles opposite to the edge in the two triangles sharing the edge $(\mathbf{x_i}, \mathbf{x_j})$ and $N_1(i)$ is the set of 1-ring neighbor vertices of vertex i. The mean curvature value is computed by taking half of the magnitude of 3.1.

Discrete Gaussian Curvature Operator

They use the same arguments as described in the discrete mean curvature operator section to argue that the Voronoi cell of each vertex is an appropriate local region to use for good error bounds. Thus, they arrive at their definition of the Gaussian curvature discrete operator:

$$\kappa_G(\mathbf{X_i}) = (2\pi - \sum_{j=1}^{f} \theta_j)/A_{mixed} \tag{3.2}$$

where θ_j is the angle of the j-th face at the vertex $\mathbf{x_i}$ and f is the number of faces around that vertex.

Principal Curvatures and Axes

Now that they have both the mean and Gaussian curvatures for triangulated surfaces, they can define the discrete principle curvatures.

$$\kappa_1(\mathbf{x}_i) = \kappa_H(\mathbf{x}_i) + \sqrt{\Delta(\mathbf{x}_i)} \tag{3.3}$$

$$\kappa_2(\mathbf{x}_i) = \kappa_H(\mathbf{x}_i) - \sqrt{\Delta(\mathbf{x}_i)} \tag{3.4}$$

where $\Delta(\mathbf{x}_i) = \kappa_H^2(\mathbf{x}_i) - \kappa_G(\mathbf{x}_i)$ and $\kappa_H(\mathbf{x}_i) = \frac{1}{2}||\mathbf{K}(\mathbf{x}_i)||$.

They find the two orthogonal principal curvature directions by computing the eigenvectors of the curvature tensor. The mean curvature can be viewed as a quadrature that uses each edge as a sample direction. By doing so, they can use these samples to find the best fitting ellipse so that the curvature tensor can be fully determined. They then find that the two principal axes are the two orthogonal eigenvectors of their curvature tensor.

General Overview

In summary, Meyer's *et. al* curvature code first restricts the averaging area to a family of special local surface patches that are contained within the 1-ring neighborhood of each vertex, with piecewise linear boundaries crossing the mesh edges at their midpoint. Then, it finds the precise surface patch that optimizes the accuracy of the curvature operators. These operators then take a vertex and its 1-ring neighborhood as an input and provide an estimate using equations 3.1 and 3.2. From equations 3.1 and 3.2, they then define the principal curvatures (3.3 and 3.4) and find the principal axes.

3.2 Mesh Processing

In this section, we discuss how we treat the mesh in order to achieve the most accurate Gaussian curvature values possible. Calculation of the Gaussian curvature, K_G, involves the computation of a double derivative. As a result, small fluctuations in the location of mesh points generated during the process of scanning the surface propagates dramatically during the curvature computation effectively obscuring the curvature map. In this subsection, we present a method to handle noise fluctuations to enable adequate visualisation of the Gaussian curvature map for the entire surface. To validate the method, we 3D-print and analyse a model of a synthetic surface of known principal curvatures. We show that the Gaussian curvatures obtained with

the proposed smoothing techniques are strikingly close to the synthetic case except for very small values of K_G.

Surface Construction

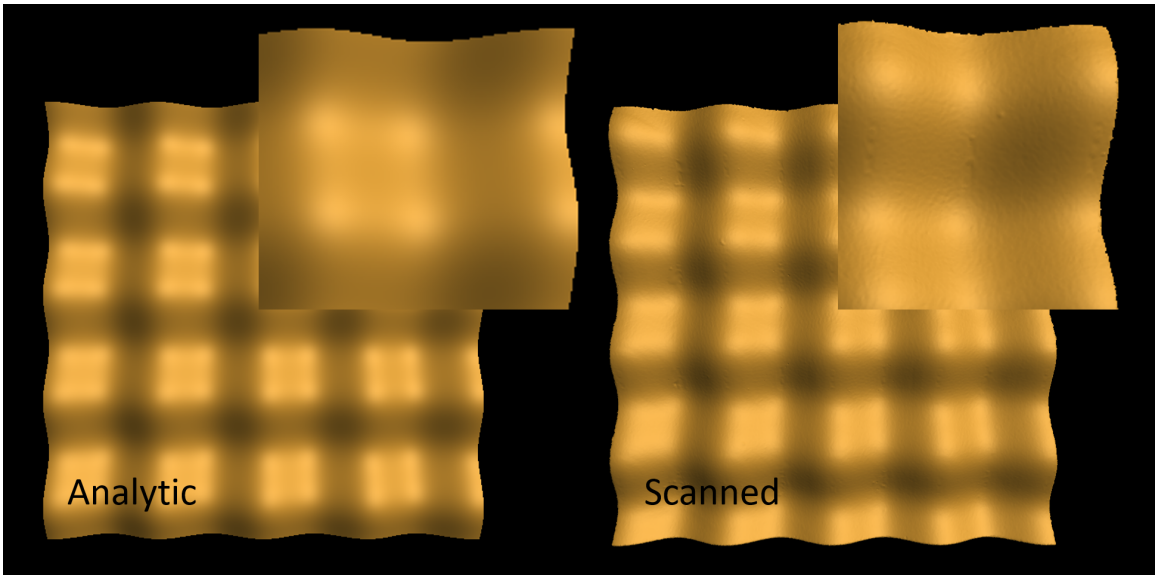

Figure 3.1: Image of the synthetic surface mesh and 3D scanning of the 3D printed surface.

The main surface we created is a periodic synthetic structure that resembles an egg-crate with peaks and basins of equal height and depth above and below the mean height. A representation of this surface is shown in figure 3.1. By design, the Gaussian curvature everywhere on this surface falls within the range $[-0.01, 0.01]$ mm^{-2}. A color map of the Gaussian curvature for the entire surface is shown in figure 3.2, where the colors range from dark-red representing peaks and basins of positive K_g, to dark-blue representing saddle points of negative K_g. The parabolic points appear green in the color map. The distribution of the Gaussian curvature for this surface is shown in figure 3.3. Note that the frequency is symmetric around zero and decays towards its extreme values.

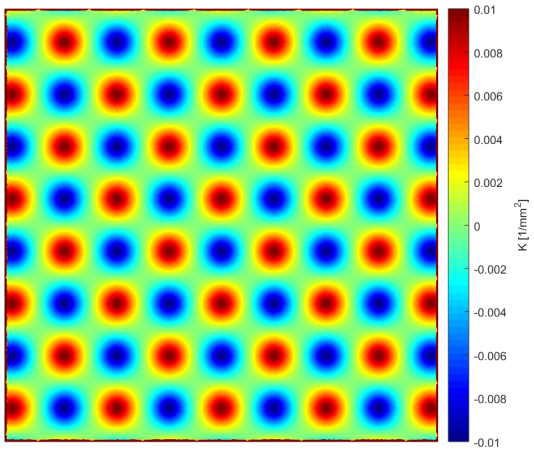

Figure 3.2: Gaussian curvature color map for the analytic surface.

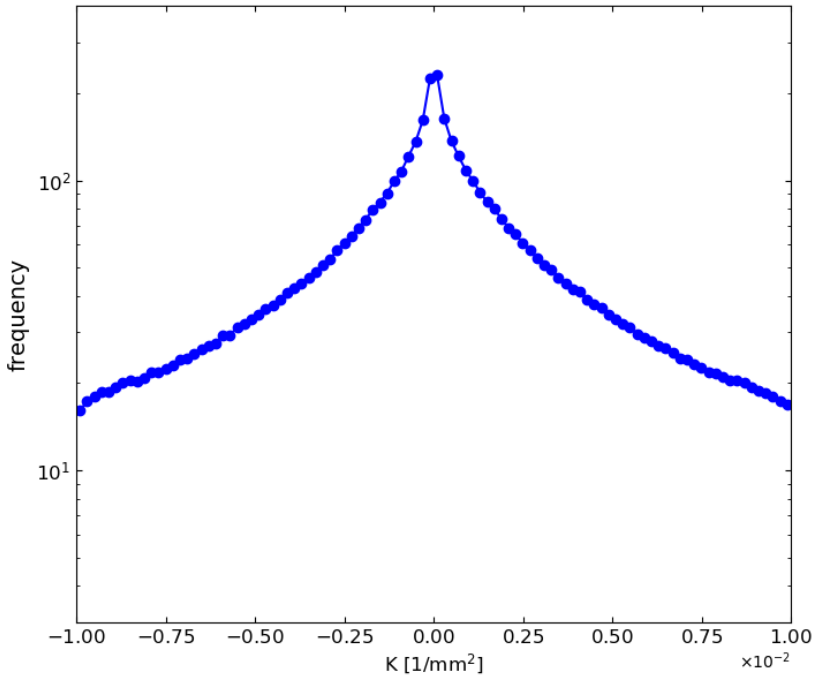

Figure 3.3: Distribution of Gaussian curvature for the analytic surface.

To study noise fluctuations generated in the process of scanning 3D surfaces, we convert the the egg-crate synthetic surface into an 3D model to be printed in

a stereolithography printer (Form 2, Formlabs). We use Formlabs' *Tough resin* (FLTOTL05), chosen for its desirable mechanical and structural properties. The printing was done at the finest possible resolution, 25 μm layer, to achieve the best printing quality. After curing, the surface was air-sprayed with a thin layer of white acrylic paint to cover the reflective surface of the resin to improve 3D imaging and subsequent reconstruction of the surface.

The printed surface was then scanned by an EinScan Pro 2X Plus scanner, which identifies points on the surface with 40 μm accuracy. We performed a fixed auto 3D scan of the surface by taking snapshots every 6 degrees (60 steps over a 360 degree scan). In post-processing, an *unwatertight* mesh model was generated from the point-cloud and edited within the scanner software to crop undesirable features such as support pillars and floating islands. Subsequently, holes on the surface were identified and individually filled using the *tangent mode* in the scanner software that calculates the patching solution based on the point position and the normal of the last row of triangles forming the boundary. The final mesh was then processed with point distance resolution of 0.2 mm, the highest available for the instrument and the output file was then saved in stereolithographic format (.stl) for further analysis.

Figure 3.1b shows a rendering of the scanned mesh surface next to the synthetic surface under artificial shading to enhance visualization of texture details. The rendering is performed in MeshLab. A close comparative inspection reveals small features on the scanned surface not present on the perfectly smooth surface of the synthetic model. These small features were generated during the printing and scanning steps and, as it will be shown later, are the source of noise in the curvature calculation.

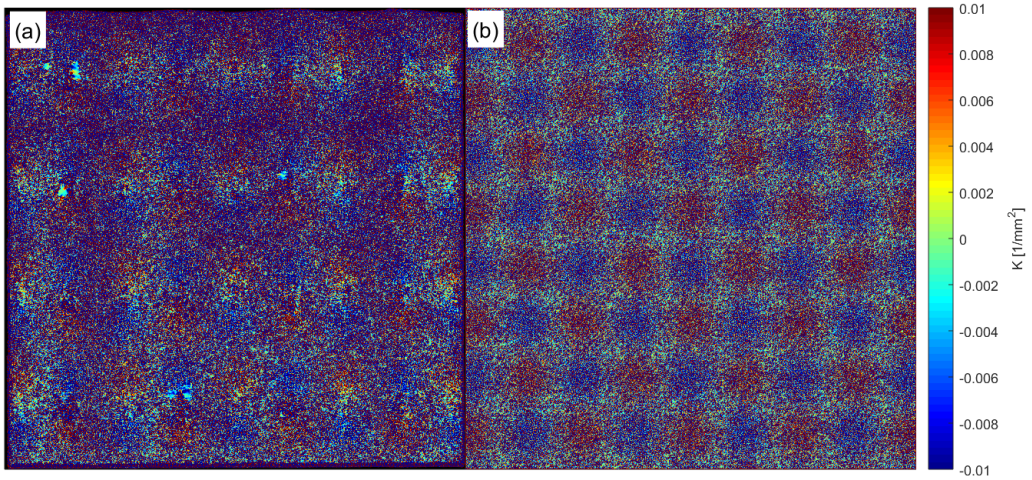

Figure 3.4: Color map of Gaussian curvature for (a) scanned surface and (b) synthetic surface plus noise.

We now turn to the comparative analysis of the Gaussian curvature for the printed and synthetic surfaces.

Gaussian Curvature Analysis of Surfaces

The computation of the Gaussian curvature for every point on the scanned surface was performed with a method by Meyer et al. [10] and implemented in MatLab by Dastan [23] as described in section 3.1. Figure 3.4a shows the color map of the Gaussian curvature for the scanned surface. In contrast with clear regions of the synthetic surface of figure 3.2, the curvature map of the scanned surface is fuzzy and barely captures the periodicity of K_G. Note that in this view the holes filled in the editing steps are easily spotted as small patches of constant Gaussian curvature. The blurring observed in the color map emerges from fluctuations in the position of the mesh points. To mimic these fluctuations, we introduced random noise to the coordinate position of the mesh points of the synthetic surface to a maximum amplitude of 0.008 mm, which corresponds to the product of the accuracy and the

resolution of the scanner. The color map of the noise-laden synthetic surface is shown in figure 3.4b. The similarity is striking and the features are indistinguishable except for the patches on the scanned surface. The Gaussian curvature distribution for both surfaces shown in figure 3.5 also looks identical indicating that fluctuations in the mesh points are indeed the source of the noise in the Gaussian curvature map. Furthermore, the mean and variance of the two curves are essentially the same as shown on table 3.1.

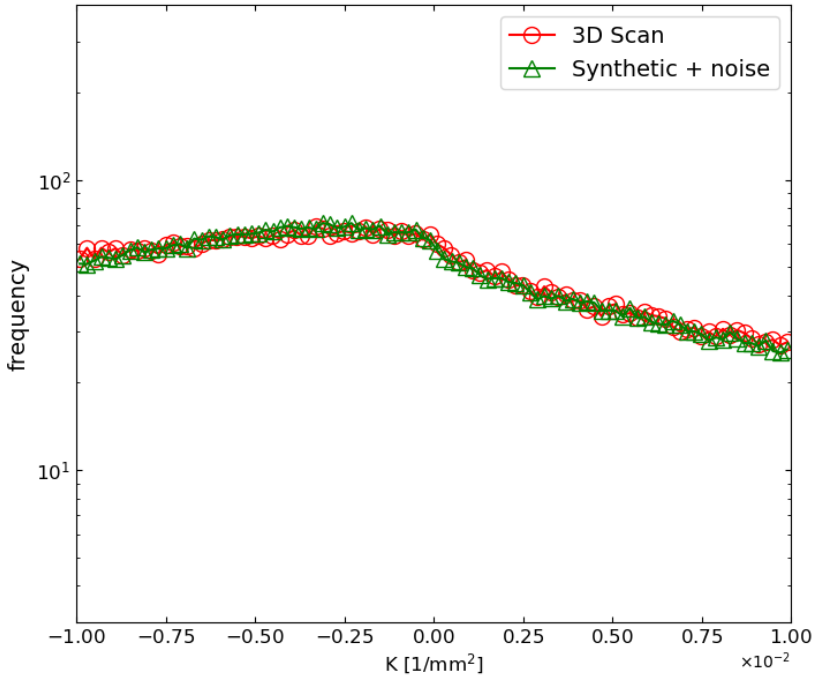

Figure 3.5: Distribution of Gaussian curvature for the raw scanned surface and the noise-laden synthetic surface.

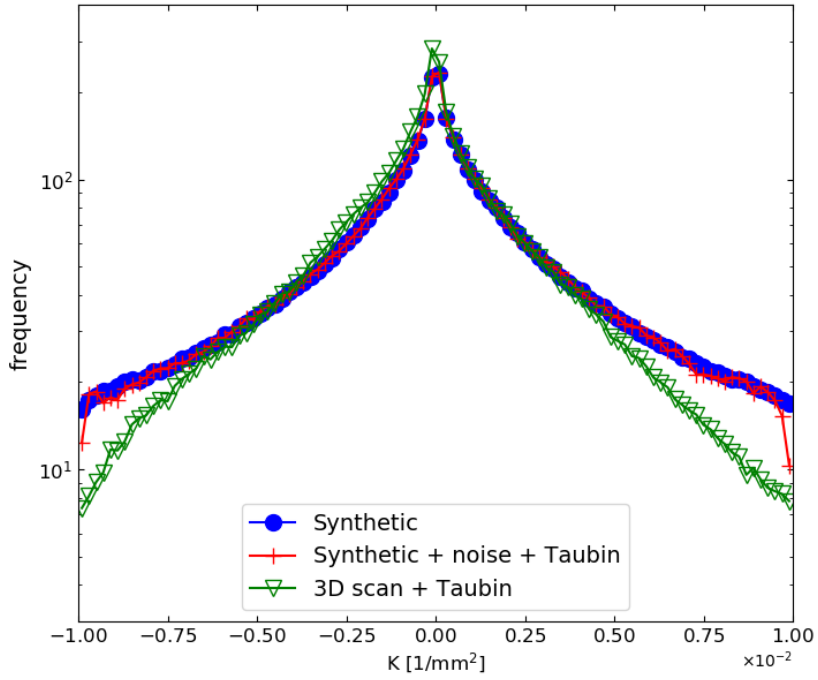

Figure 3.6: Distribution of Gaussian curvature for the original synthetic surface, the noise-laden smoothed synthetic surface, and the smoothed scanned surface.

Data	Mean	Variance	Skewness	Kurtosis
Synt.	5.421E-06	4.077E-03	-2.460E-04	6.834E-02
Synt. + n	-1.412E-03	5.254E-03	3.431E-01	-8.458E-01
Synt. + n + T	-3.324E-06	4.029E-03	-5.827E-03	8.384E-02
Sc.	-1.362E-03	5.306E-03	3.181E-01	-8.768E-01
Sc. + T	-1.995E-04	3.531E-03	2.081E-02	5.147E-01
Sc. + T + 2xL	-7.027E-05	3.650E-03	2.806E-02	3.245E-01

Table 3.1: Table of statistical data of Gaussian curvature distribution for the synthetic and scanned surfaces with noise and smoothing.

The fact that random noise added to synthetic surface captures so well the nature of the fluctuations present on the scanned surface suggests that surface smoothing for noise reduction is the first step to improve visualization of the Gaussian curvature on the surface.

Gaussian smoothing, based on computing weighted averages of neighboring vertices, is a popular method of noise reduction of geometric surfaces. Since the number of operations scales linearly with the number of vertices in the surface, Gaussian smoothing is computationally inexpensive and can be applied multiple times iteratively to achieve long range smoothing but with the side effect of causing significant shinkrage, specially when applied multiple times. Taubin [11] proposed a solution to this problem by implementing two Guassian smoothing steps, one with a positive scale factor λ followed by another with negative scale factor μ, but greater in magnitude than λ to suppress the shrinkage. When applied multiple times, the method can be thought of as a low-pass filter that effectively attenuates the high-curvature fluctuations that plague scanned surfaces.

The Taubin smoothing method described above has been efficiently implement in MeshLab and we use this open-source software to smooth both the noise-laden synthetic and scanned surfaces with parameters $\lambda = 0.80$, $\mu = -0.83$ and $N = 100$. Note that the results of Taubin smoothing is not very sensitive to the specific choice of parameters as long as the number of iterations is large. Figure 3.6 shows the distribution of Gaussian curvature for the scanned surface, the noise-laden synthetic surface and the pure synthetic surface. Not surprisingly, the Taubin smoothing procedure restores the randomized surface to its original distribution except for small deviations at the tip of the tails. For small to moderate curvature, the K_G distribution for the smoothed scanned surface follows the distribution of the synthetic surface except for a slight excess of negative K_G, but for larger curvatures the surface experiences stronger attenuation. Since the original noise levels for both the synthetic and scanned surfaces were the same, we conclude that large curvatures gets attenuated during the 3D printing and scanning stages.

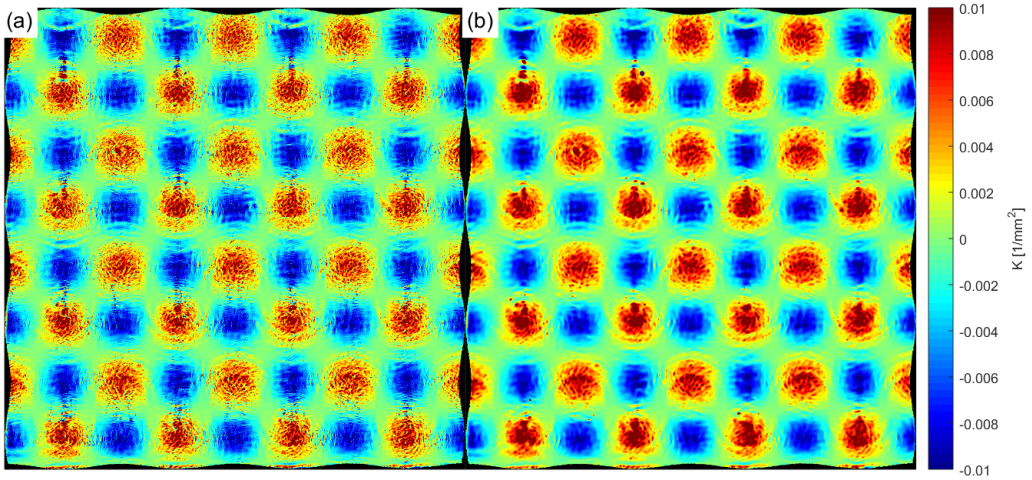

Figure 3.7: Gaussian curvature color map for the scanned surface after (a) Taubin smoothing and (b) Taubin smoothing and 2 steps of Laplacian smoothing.

Figure 3.7a shows the Gaussian curvature color map for the scanned surface treated with Taubin smooth. It is remarkable how local regions of positive and negative K_G are recovered with this simple step. Even fine details such as the micron-size steps of printing layers are discernible in between the peaks. However, the mean value of the distribution of the smoothed surface is much removed from the expected zero mean as compared with the original synthetic surface. We address this problem by performing 2 steps of a simple Laplacian smoothing of the local Gaussian curvature field with reduces the mean of the K_G distribution by two orders of magnitude falling much closer to the expected zero mean. Indeed, figure 3.7b shows how this smoothing step enhances the clusters of positive and negative Gaussian curvatures. The details of these steps can be more clearly seen in figure 3.8 where the Gaussian curvature color map of the scanned surface subject to Taubin smoothing, and Laplace smoothing can be compared with that of the synthetic surface.

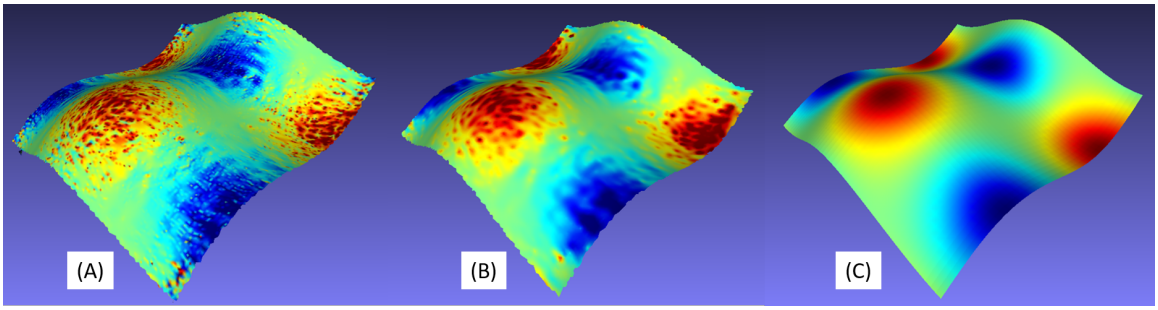

Figure 3.8: Comparative Gaussian curvature color map for (a) scanned surface with Taubin smoothing, (b) scanned surface with Taubin smoothing and 2 steps of Laplacian smoothing, (c) the analytic surface.

4 Analysis of Curvatures

In this chapter, we discuss the results obtained from the mean and Gaussian curvature calculations. First, we analyze the mean and Gaussian curvatures over a portion of the buckled surface containing multiple protruding vertices. Next, we focus on the Gaussian curvature charge of single protruding vertices. Finally, we determine the minimum width across single protruding vertices and analyze the trend across all thickness.

4.1 Mean Curvature

We compute the mean curvature because its presence is indicative of how much bending energy is contained within the surface. The result is show in figure 4.1 which reveals that negative curvature dominates the ridges while the positive curvature is confined to the interior of the unit cells. As thickness decreases, the colors indicative of mean curvature become deeper, indicating that there is an increase of bending energy. The lobes also appear smaller and the ridges sharper as thickness decreases. The pattern remains relatively uniform for all thicknesses, excluding shells of thickness 2.5μm and 6μm. The irregularities in both 2.5μm and 6μm are due to the extremely thin nature of the sheet; there might be a considerable frictional force between the Mylar and the PVC tube that prevents the pattern from forming uniformly.

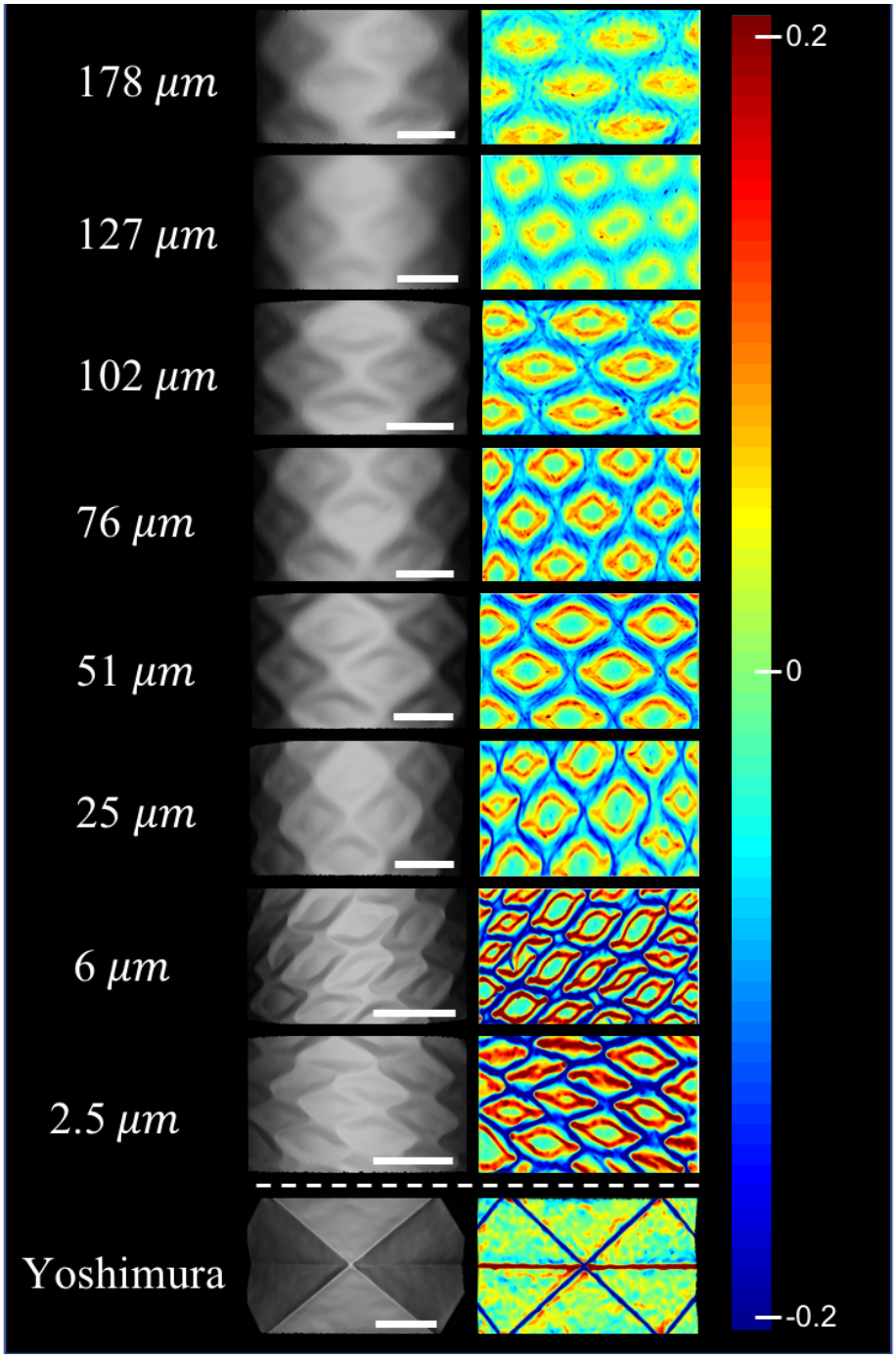

Figure 4.1: Comparison between section of scanned shells and mean curvature for sheets of different thicknesses. Scale bars are 10000 μm.

4.2 Gaussian curvature

In order to understand how stress localizes as we decrease the thickness of our shell, we must consider the stretching energy, and thus the Gaussian curvature.

Large Sections

We compute the Gaussian curvature because its presence is indicative of how much stretching energy is contained within the surface. The result is shown in figure 4.2 which reveals multiple trends. We observe that the Gaussian curvature color map displays increasingly localized features, more closely resembling the Yoshimura pattern as thickness decreases. The colors indicative of Gaussian curvature become deeper as thickness decreases, illustrating that the curvature charge substantially increases from the thickest to the thinnest shell. This trend is what we expected to see; increasingly localized stresses should have a higher Gaussian curvature. We also note that the highest regions of Gaussian curvature become increasingly localized on and around the protruding vertices as thickness decreases. The positive Gaussian curvature is majority concentrated on the apex of the vertices while the negative Gaussian curvature is focused on the interiors of the protruding vertices. It is important to note that the overwhelming majority of the positive and negative Gaussian curvature charges become increasingly concentrated on and around the protruding vertices as thickness decreases, while the rest of the buckled pattern contains majority zero Gaussian curvature. This indicates that as thickness decreases, stress becomes increasingly localised on and around the protruding vertices, as expected.

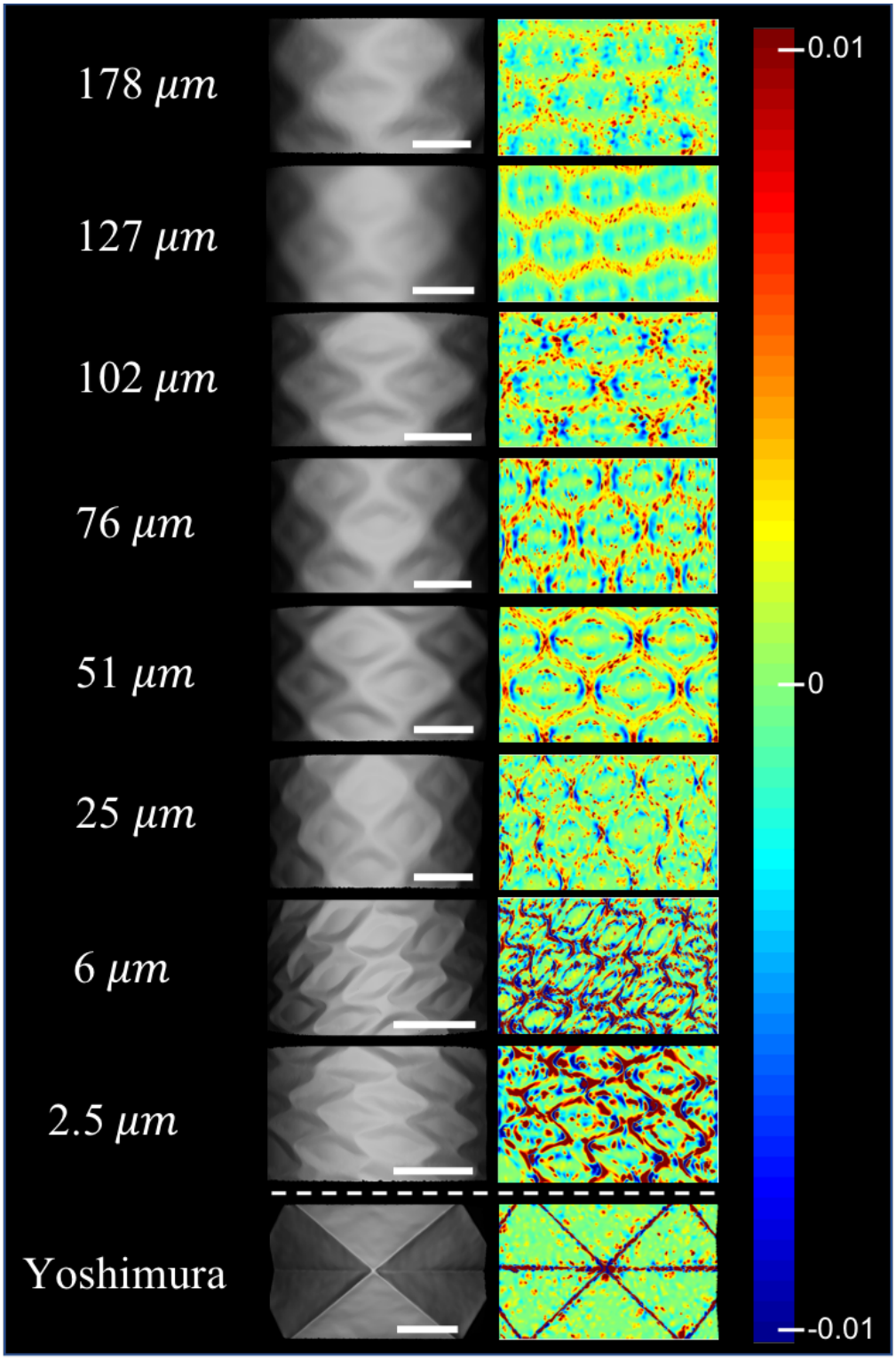

Figure 4.2: Comparison between section of scanned shells and Gaussian curvature for sheets of different thicknesses. Scale bars are 10000 μm.

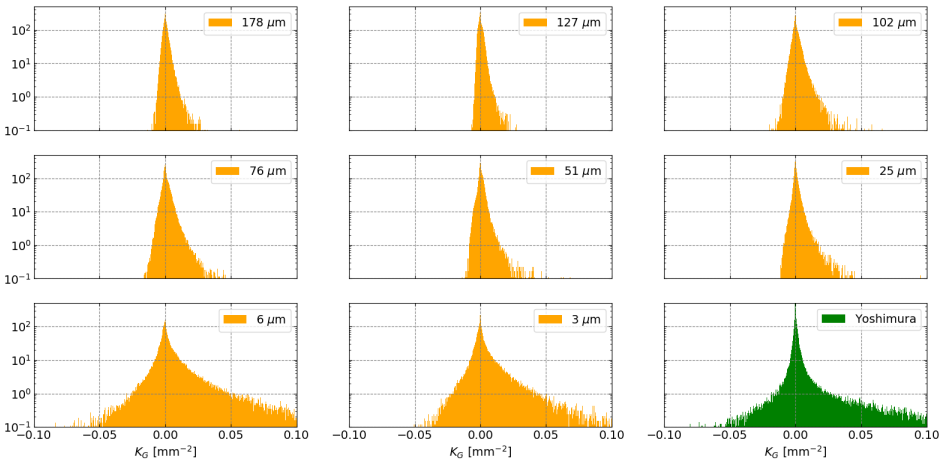

Figure 4.3: Probability density vs. shell thickness.

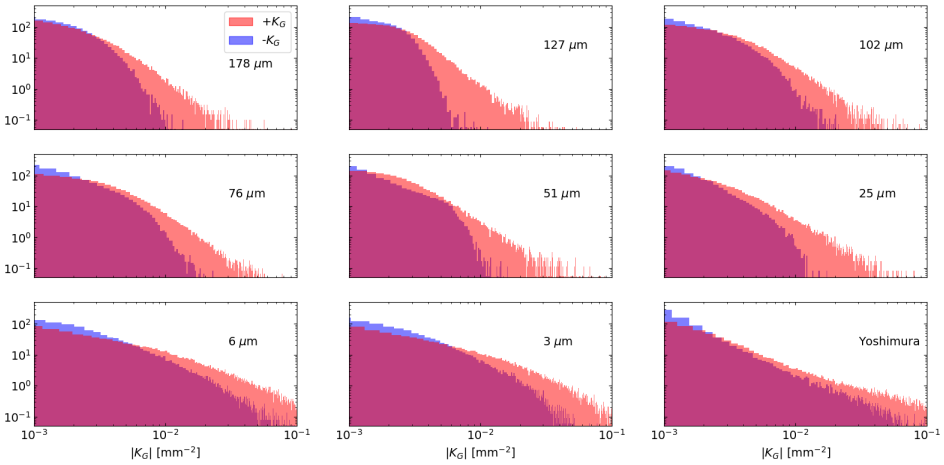

Figure 4.4: Probability density vs. shell thickness with negative and positive Gaussian curvature values superimposed.

We further analyzed our data by plotting the probability density of the average Gaussian curvature (Fig. 4.3). There is a clear trend in which the distribution broadens as the shell thickness decreases. This indicates that as the thickness decreases, there is an increasing amount of extreme Gaussian curvature charges. Note that in all cases, there is more positive Gaussian curvature than negative (Fig. 4.4). Figure

4.4 displays an interesting trend; as the thickness decreases, the distribution broadens and there is a decrease in the difference between positive and negative Gaussian curvature. The decrease in Gaussian curvatures appears linear, indicating that, at high curvatures, the distribution is approaching a power function of the Gaussian curvature as thickness decreases.

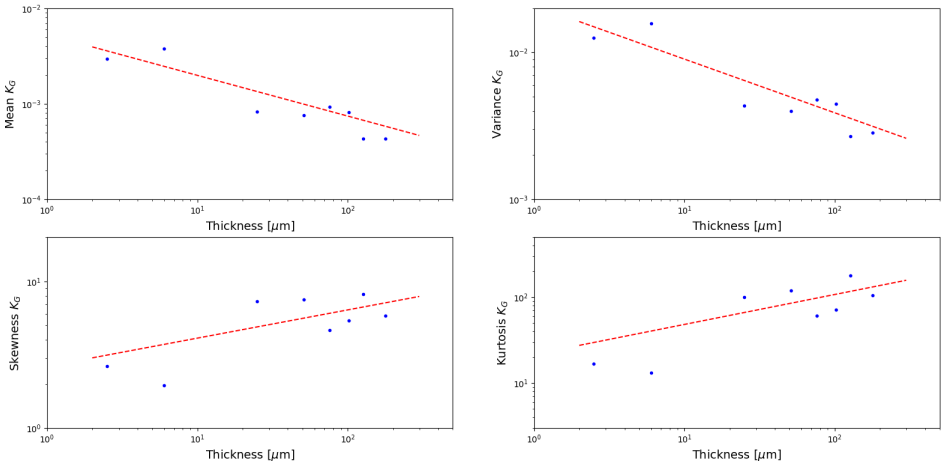

Figure 4.5: Mean, variance, skewness, and kurtosis plots of figure 4.3

We analyze the statistics behind figure 4.3 and fit a power law to the data (Fig. 4.5) to guide the eye. We see that both the mean and variance increase as thickness decreases. We expect the variance to increase as the thickness decreases because the protruding vertices become sharper and generate more Gaussian curvature. It is not clear why the mean is increasing. This will be a topic of future investigation.

In contrast, the skewness and the kurtosis increase as thickness increases. Skewness measures how symmetric or asymmetric a distribution is. We see in figure 4.5 that skewness is decreasing with thickness; this suggests that excess positive Gaussian curvature becomes balanced by negative Gaussian curvature as the shells approach the isometric limit. Kurtosis measures the contribution of outliers to the distribution. The kurtosis for all thicknesses is above 3 but the values decrease as thickness

decreases. This indicates that the distribution is better behaved for thinner shells.

Next, we focus on the Gaussian curvature of single protruding vertices.

Single Protruding Vertices

Figure 4.6 highlights individual protruding apexes from each thickness. Qualitative analysis of figure 4.6 reveals that as thickness decreases, the Gaussian curvature charge of a single protruding vertex more closely resembles the Gaussian curvature charge of the Yoshimura pattern– an increasing amount of Gaussian curvature becomes more concentrated in an increasingly smaller area. This suggests that our isometric limit may be represented by the isometric construction. The Gaussian curvature color maps (Fig. 4.6) also reveal that an increasing amount of negative Gaussian curvature develops around the protruding vertex as thickness decreases. As thickness decreases, we note that there is an unanticipated rich display of secondary structures surrounding the vertices. Around the vertices, we observe an area of positive curvature bookended by regions of negative curvature. This pattern represents a complex interplay of positive and negative Gaussian curvature surrounding the protruding vertices. Underlying the more prominent interplay of positive and negative Gaussian curvatures, we find a more complex substructure with small islands of positive Gaussian curvature on both sides of the vertex. This result reveals a complex interplay between stresses and geometrical constraints in the Mylar sheet.

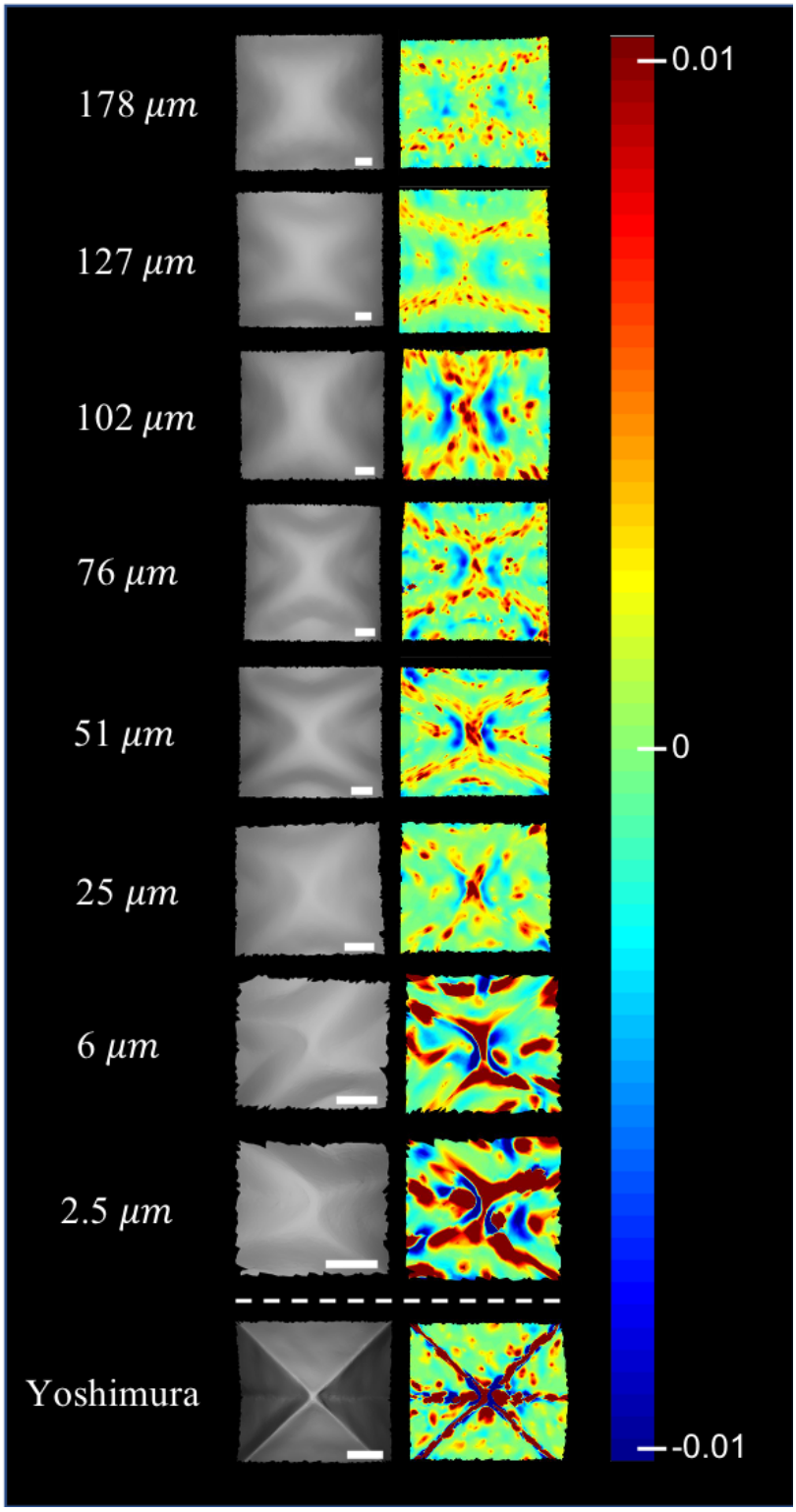

Figure 4.6: Comparison between scanned vertices and Gaussian curvature for sheets of different thicknesses. Scale bars are 2000 μm.

Protruding Vertex Width

For thinner shells, features of the buckling pattern get more localized. We estimate the degree of localization by computing the minimum width of the protruding vertices. The method is as follows.

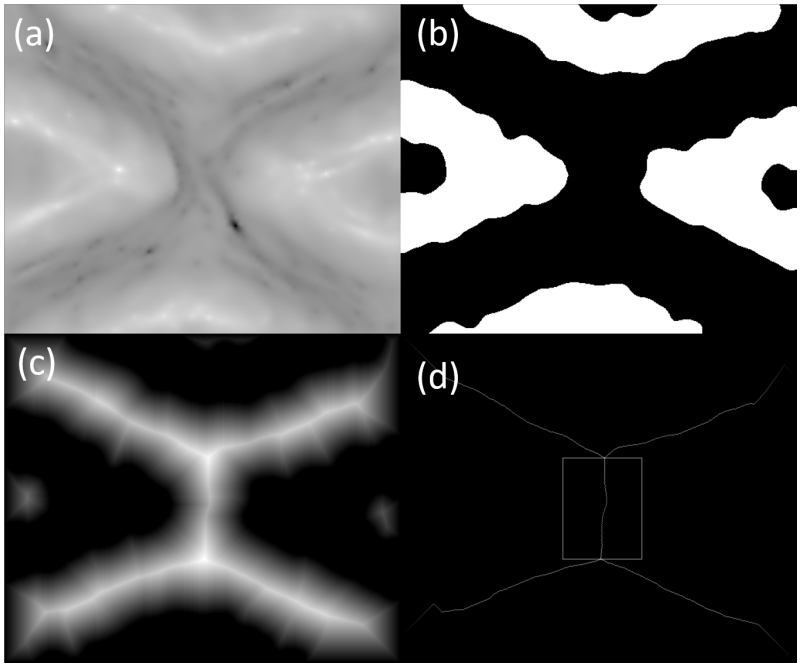

Figure 4.7: (a) Greyscale mean curvature map of 50 μm shell, (b) mean curvature map where black represents positive mean curvature values and white represents negative mean curvature values, (c) Euclidean Distance Map (EDM) of positive mean curvature values, (d) lowest point in the ridge corresponding to shortest width of protruding vertex.

First, we compute the mean curvature of the section containing the vertex of interest as described in chapter 3. Next, we convert the mesh into an image by interpolating the x,y coordinates of the mesh points into a 2D grid whose values correspond to the mean curvature (Fig. 4.7a). The image is then segmented into positive (black) and negative (white) curvature regions. Our goal is to determine the minimum thickness of the central black region (Fig. 4.7b). For that we compute the Euclidean Distance Map (EDM) of the black region, which essentially assigns for each

foreground pixel its distance to the nearest background pixel. The result is shown in figure 4.7c. To find the minimum distance, we focus our attention on the ridge line between the bifurcation points and locate the minimum point in the ridge (Fig. 4.7d).

A series of image manipulations are performed at this step. First, we skeletonize the EDM image to restrict our search to the ridge only. Then we identify the bifurcation points by convolving the image with a neighbor summing kernel. Finally, we search for the point of minimum for the section of the ridge located between the two forks. By construction, the minimum corresponds to twice the width of the vertex.

We repeat this process for 5 different vertices for each shell. The mean width of the vertex is shown on Table 4.1.

Thickness (μm)	Minimum Feature Width (mm)	Uncertainty (mm)
178	5.21	0.15
127	3.91	0.45
102	3.86	0.48
76	3.22	0.32
51	2.33	0.60
25	1.59	0.13
6	0.74	0.05
2.5	0.68	0.06

Table 4.1: Table of minimum protruding vertex width for each thickness.

We plot the results of table 4.1 in figure 4.8.

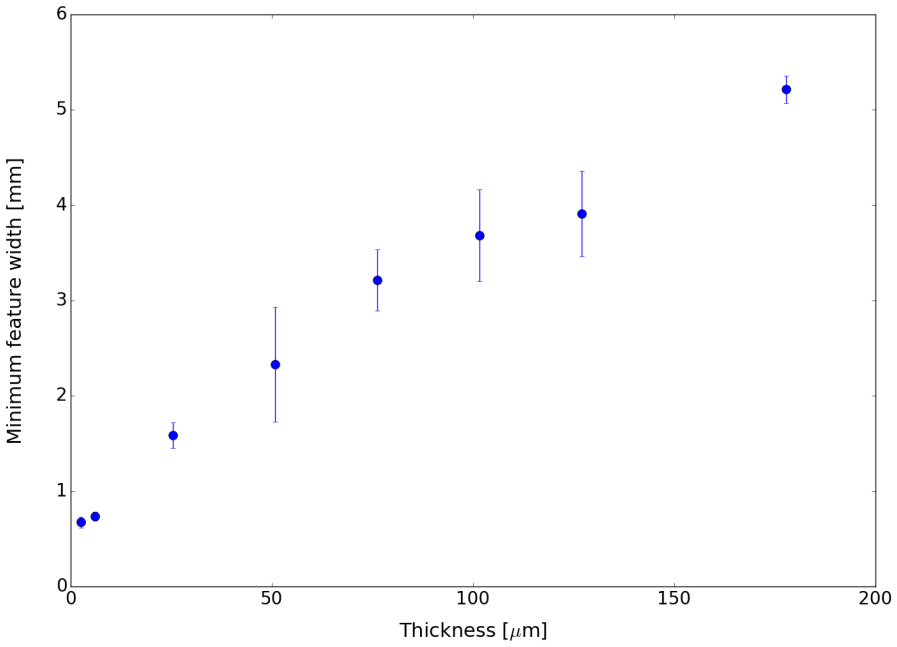

Figure 4.8: Plot of the minimum protruding vertex width against shell thickness.

Figure 4.8 shows a clear, almost linear, trend. As thickness decreases, the minimum protruding vertex width decreases. This reveals that stress is becoming increasingly localized as the shell thickness decreases.

5 Numerical Simulations

To confirm our experimental results, we simulate our buckling problem using finite element methods [12]. First, we digitally construct the cylindrical shell. Then, we implement imperfections to achieve nonlinear behavior. Finally, we simulate the buckling process in ABAQUS.

5.1 Model Construction

The cylinder was constructed with length $L = 127$ mm and diameter $D = 61.39$ mm. We assume that the material of the shell has a linear elastic behavior with a Young's modulus of 2.5 GPa and a Poisson ratio of 0.38. The gap between the cylindrical shell and inner constraint was set to be 0.8 mm. A surface-to-surface discretization method with finite sliding was used to model the contact between the shell and inner support. Both surfaces were allowed to slide freely without friction but an Augmented Lagrangian method was implemented to enforce contact constraints. We set the outer of the inner support as the master surface and the inner of the cylindrical shell as the slave surface.

We use the transversal plane in the middle of the cylinder as the plane of symmetry; this is allowed due to the compression experienced at both ends. The presence of this plane of symmetry enables us to model only half of the cylinder, greatly reducing the computational effort. A reference node is set in the plane of symmetry along the axis of the cylinder and connected with rigid links to all of the nodes placed in the plane of symmetry. Symmetric boundary conditions are applied on this reference node. Due to the rigid links, these symmetric boundary conditions are then simultaneously applied to all of the nodes on the plane of symmetry.

We set another reference point along the axis of the cylinder, again connecting it to the nodes placed on the end of the cylinder with rigid links. An imposed displacement

boundary condition in the direction of the axis of revolution is applied to this node and transmitted to the other end nodes, causing the cylinder to compress.

The post-buckling analysis is a nonlinear problem, but we have made the assumption that the material used is linearly elastic. Thus, the material cannot be the source of this nonlinearity; in fact, the geometry of the model is the source. The model is not a perfect cylinder as there are some small imperfections in it, so we must implement these imperfections into the cylinder mesh in order to achieve the correct post-buckling behavior.

Implementation of Imperfections

We use a the Linear Buckling Mode-shape Imperfection (LBMI) [21] method to introduce these imperfections into our mesh. LBMI perturbs the original mesh by scaling its mode shapes by a factor. This can be seen as a small translation of the nodal coordinates from the original mesh in Finite Element Method:

$$\delta x = \sum_{k=1}^{n} w_k \phi_k. \tag{5.1}$$

Here, ϕ_k represents the mode k or the mesh, while w_k represents the scaling factor associated to that mode.

In general, the lowest mode carries the highest scaling factor. We use this assumption and starting from $w_1 = 0.05$, we calculate every scaling factor as $2w_k = w_{k-1}$. The first three modes are used to model the imperfections. In order to determine the mode shape used to perturb the mesh, we implement a simple Linear Modal Analysis (LMA) in ABAQUS for the original mesh. We only use the first three modes because the scaling factor, and the effect of the mesh perturbation, decreases exponentially. The accuracy of this model is checked by studying the post-buckling of a one-dimensional beam under axial compression.

Beam under Axial Compression

The behavior of a one-dimensional bean under axial compression is well known. The critical load for the first buckling mode is given by

$$P_{cr} = \frac{\pi^2 EI}{L^2}.$$

The normalized Load-Displacement curve obtained by the numerical simulation for this problem is shown in figure 5.1. It is obvious that the buckling behavior occurs when the load is critical.

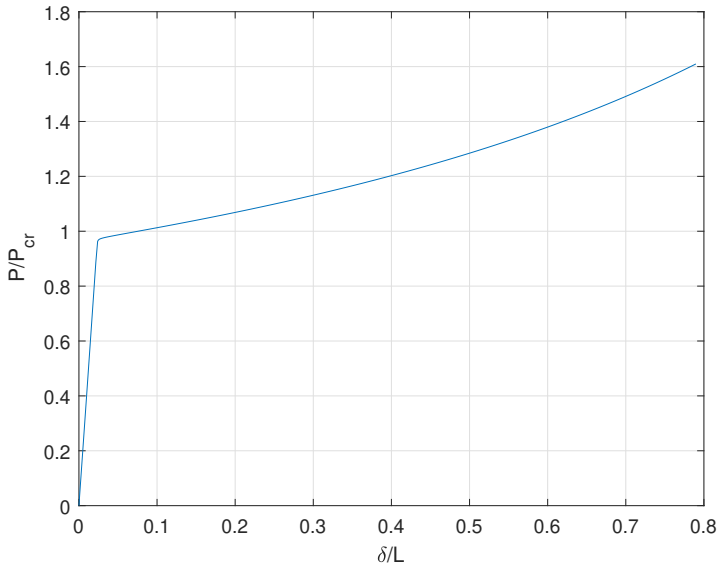

Figure 5.1: Normalized load-displacement curve for a beam under axial compression.

The normalized maximum deflection at the middle of the beam is plotted as a function of the load (Fig. 5.2). We see that the deflection is zero until the load reaches the critical value and then it grows suddenly, again highlighting the effect of buckling.

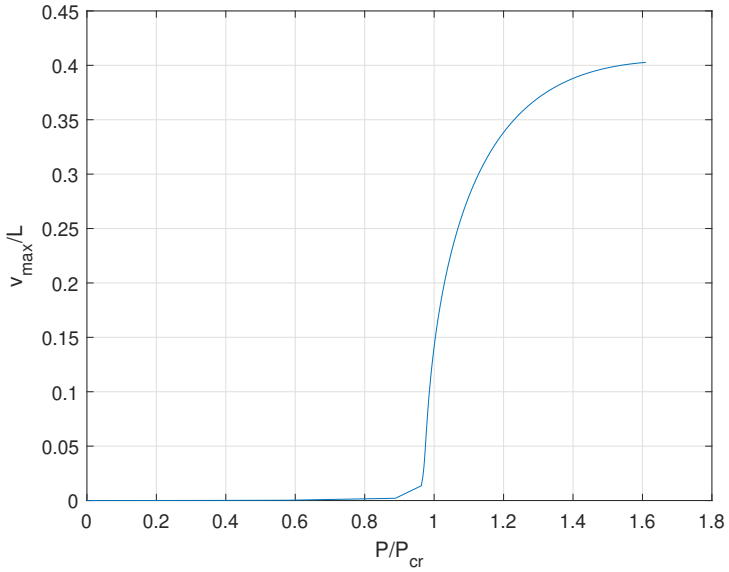

Figure 5.2: Normalized maximum deflection of the beam as a function of the compressive force.

The results from this problem show that the procedure used in implementing imperfections and the post-buckling analysis is consistent with theory. Thus, we now approach the main problem of our work.

Post-buckling Analysis

After the modes are obtained and the original geometry is perturbed, a post-buckling analysis is performed. We perform the post-buckling analysis using a displacement control method on the top reference node, which transmits the displacement to all of the top edge nodes through rigid links. The shell is compressed until a displacement of 1.5 mm is applied on the top edge nodes. Then, a load-displacement curve is obtained and the mean and Gaussian curvature fields are calculated over the deformed shell.

5.2 Numerical Implementation

This problem is solved using the Finite Element software ABAQUS. The thin cylindrical shell is modeled with an S8R shell element. This allows a quadratic displacement

field calculation along the shell which results in a more accurate model and fine results, even for coarse meshes. The inner support is modeled using R3D4 elements. Given that the inner cylinder is rigid and does not deform, this element is not relevant to our study. However, its mesh must be refined enough so that the contact algorithm produces accurate results. We use structural meshes along both the thin shell and inner support because, initially, it is not known whether a pattern will appear or which regions of the shell are the most deformed.

We parametrize the size of the elements as a factor of the radius of the cylinder, having the coarser mesh be of side length $R/10$ and the most refined mesh be of side length $R/30$.

5.3 Results

In this section, we discuss the results obtained from the Gaussian curvature calculations of the simulated buckled shell. We analyze the Gaussian curvature over a portion of the buckled simulation surface that contains multiple protruding vertices.

Analysis of figure 5.3 reveals similar trends to those displayed in figure 4.2. We plot the probability density of the average Gaussian curvature (Fig. 5.4) and find that the distribution broadens as shell thickness decreases. This matches the results shown in figure 4.3; thus, we confirm that there is an increasing amount of extreme Gaussian curvature charges as the thickness decreases.

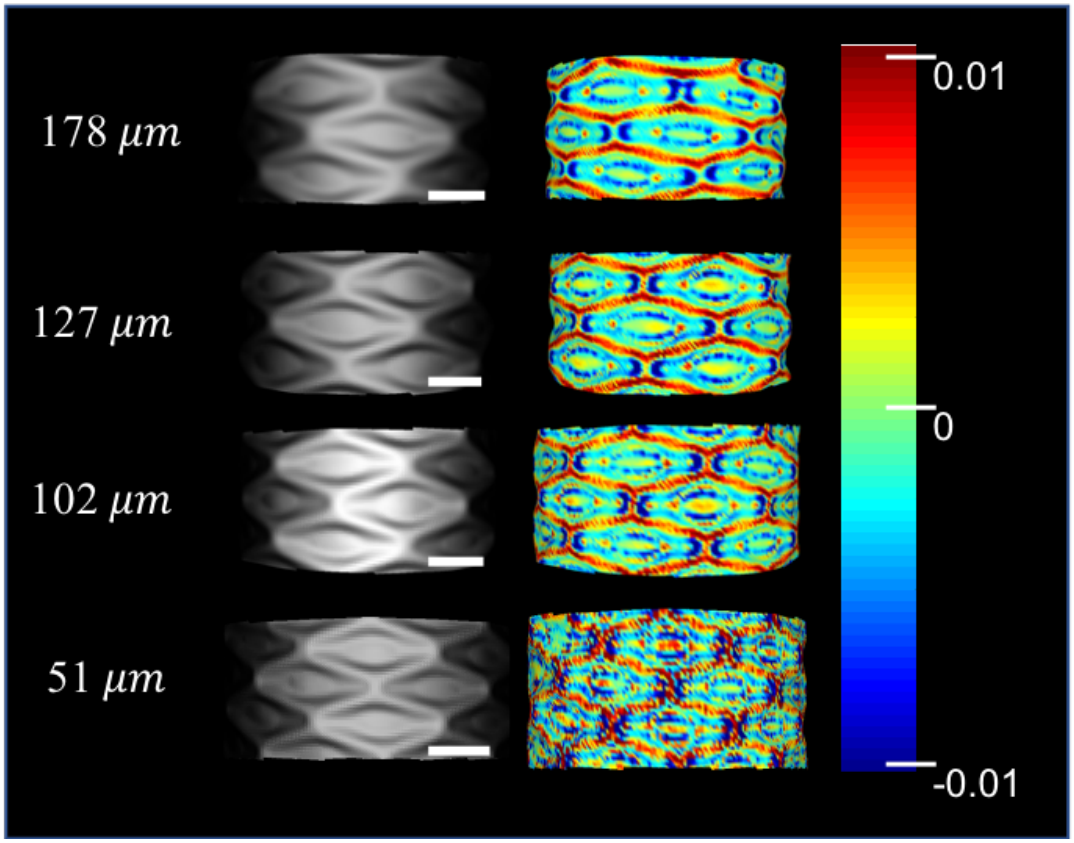

Figure 5.3: Comparison between sections of simulated shells and Gaussian curvature for sheets of different thicknesses. Scale bars are 10000 μm.

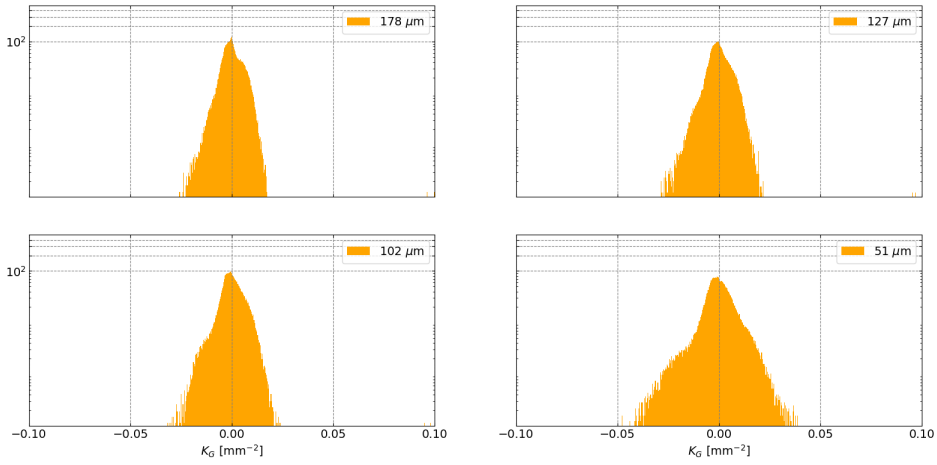

Figure 5.4: Probability density vs. shell thickness.

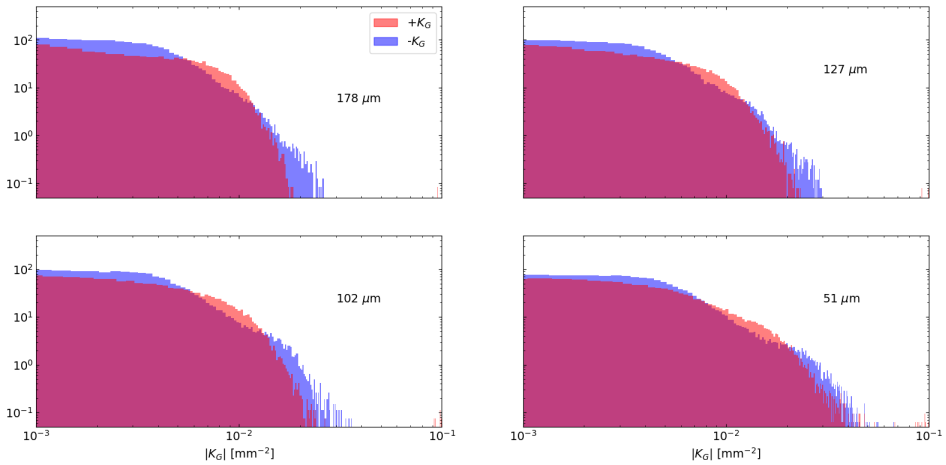

Figure 5.5: Probability density vs. shell thickness with negative and positive Gaussian curvature values superimposed.

The probability density shown in figure 5.5 displays the same trend of the experimental data seen in figure 4.4. We observe that as thickness decreases, there is a decrease in the difference between positive and negative Gaussian curvature. However, we note that there is always more negative Gaussian curvature than positive in figure 5.5, whereas figure 4.4 always displays more positive Gaussian curvature than negative. This discrepancy will be explored in future work.

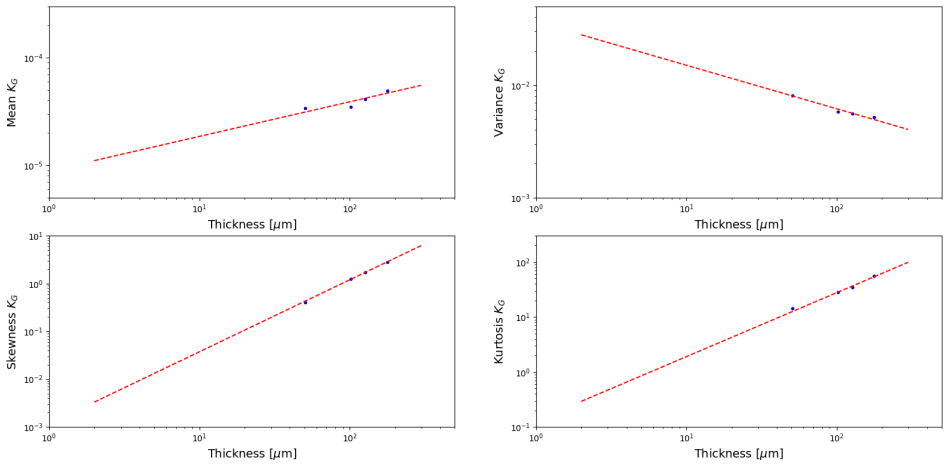

Figure 5.6: Mean, variance, skewness, and kurtosis plots of figure 5.4.

We now analyze the statistics behind figure 5.4 and fit a power law to the data as a guide to the eye (Fig. 5.6). The power bar fits remarkably well, indicating that the distribution is indeed approaching a power function of the Gaussian curvature. We see that the variance increases as shell thickness decreases. This matches our experimental results (Fig. 4.5) and confirms that as thickness decreases, the protruding vertices become sharper and generate more Gaussian curvature.

The mean, skewness, and kurtosis increase as thickness increases. Our experimental results also show that skewness and kurtosis increase as thickness increases (Fig. 4.5). Thus, we confirm that as shell thickness decreases, excess positive Gaussian curvature becomes balanced by negative Gaussian curvature and the probability distribution of the average Gaussian curvature becomes better behaved.

We note that our experimental data shows that the mean increases as thickness decreases whereas our numerical simulation data shows that the mean decreases as thickness decreases. We expected to find the latter; we expected that, if the isometric limit is represented by the ideal Yoshimura pattern, then the mean Gaussian curvature would approach zero as thickness decreases due to the flat-foldable nature of the

Yoshimura pattern. The discrepancy between the two results will be explored in future work.

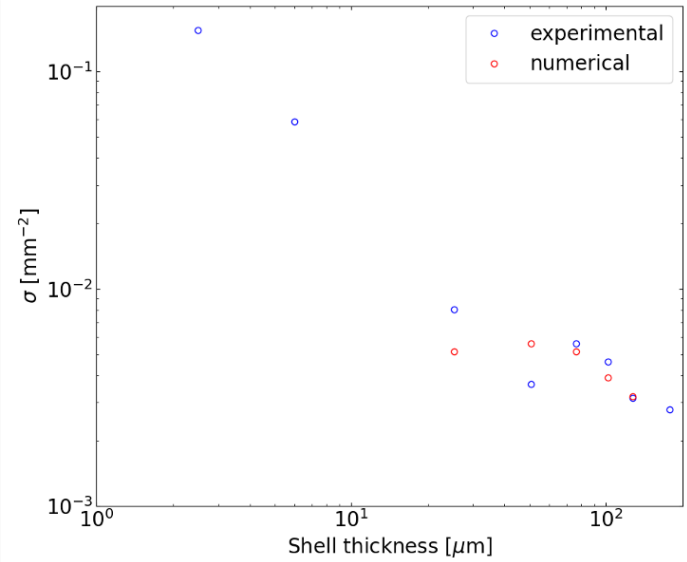

Figure 5.7: Log-log plot of the standard deviation of the average Gaussian curvature vs. shell thickness for experimental and numerical simulation data. Yoshimura pattern is not included.

Finally, we consider a log-log graph of the standard deviation of the average Gaussian curvatures verses the shell thickness (Fig. 5.7). As the shell thickness decreases, the standard deviation increases, indicating that the spread of the average Gaussian curvature broadens as we approach the isometric limit. Again, this implies that as the shell thickness decreases, an increasing amount of Gaussian curvature is contained within a smaller area. Figure 5.7 reveals an almost linear trend for both experimental and numerical simulation data. The strong agreement between the experimental and numerical data indicates that the cylindrical shells are indeed approaching the isometric limit as expected.

6 Conclusions

We have established concrete protocols in the construction, scanning, and post-processing of thin constrained cylindrical shells. We have also successfully computed the mean and Gaussian curvatures of these shells experimentally and numerically.

We have found that as shell thickness decreases, the Gaussian curvature charge substantially increases (Fig. 4.2). More precisely, the highest regions of Gaussian curvature become increasingly localized on and around the protruding vertices as thickness decreases (Fig. 4.6). This indicates that as thickness decreases, stress becomes increasingly localized on and around the protruding vertices. We found that the probability density of the average Gaussian curvature distribution broadens, showing that there is an increasing amount of extreme Gaussian curvature charges as thickness decreases (Fig. 4.3). We also note that the difference between the positive and negative Gaussian curvature distributions is decreasing as thickness decreases, indicating that the distribution is approaching a power function of the Gaussian curvature (Fig. 4.4).

Next, we analyzed the mean, variance, skewness, and kurtosis of the probability distribution (Fig. 4.5). The variance increased as thickness decreases, indicating that the protruding vertices become sharper and generate more Gaussian curvature. The skewness decreased as thickness decreases, suggesting that excess positive Gaussian curvature becomes balance by negative Gaussian curvature. The kurtosis showed that the probability distribution is better behaved for thinner shells.

An analysis of the width of the protruding vertices revealed that as thickness decreases, the minimum protruding vertex width decreases. This suggests that the stress is becoming increasingly localized as the shell thickness decreases (Fig. 4.8).

Our numerical simulations confirmed our experimental results. We note that there

is a strong agreement between the experimental and numerical simulation standard deviation values; this indicates that the spread of the average Gaussian curvature is indeed broadening as we approach the isometric limit (Fig. 5.7). We also observe that the numerically simulated variance, skewness, and kurtosis trends agree with our experimental results (Figs. 4.5, 5.6). Additionally, we find that as shell thickness decreases, the probability distribution of the average simulated Gaussian curvature increases; again, this agrees with our experimental results. However, our experimental results show that there is always an excess of positive Gaussian curvature whereas our simulations show that there is always an excess of negative Gaussian curvature. We also observe that the experimental mean decreases as shell thickness increases, whereas the numerically simulated mean increases as shell thickness increases. Both of these discrepancies will be investigated in future work.

Along with the above quantitative analyses, we found that as thickness decreases, there is an unanticipated rich display of secondary structures surrounding the protruding vertices. This reveals a complex interplay between stresses and geometrical constraints in the thin sheets. Our future work will investigate this complex interplay.

Bibliography

[1] D. Bushnell, "Buckling of shells–pitfall for designers," *AIAA Journal*, vol. 19, no. 9, pp. 1183–1226, 1981.

[2] F. Cottone, L. Gammaitoni, H. Vocca, M. Ferrari, and V. Ferrari, "Piezoelectric buckled beams for random vibration energy harvesting," *Smart Materials and Structures*, vol. 21, no. 3, 2012.

[3] J. Winterflood, T. Barber, and D. G. Blair, "Using Euler buckling springs for vibration isolation," *Classical and Quantum Gravity*, vol. 19, no. 7, pp. 1639–1645, 2002.

[4] E. Cerda, S. Chaleb, F. Melo, and L. Mahadevan, "Conical dislocations in crumpling," *Nature*, vol. 401, no. 6748, pp. 46–49, 1999.

[5] K. A. Seffen, "dcones.pdf," 2016.

[6] J. Chopin and A. Kudrolli, "Disclinations, e-cones, and their interactions in extensible sheets," *Soft Matter*, vol. 12, no. 19, pp. 4457–4462, 2016.

[7] T. A. Witten, "Stress focusing in elastic sheets," *Reviews of Modern Physics*, vol. 79, no. 2, pp. 643–675, 2007.

[8] M. Venkadesan, A. Yawar, C. M. Eng, M. A. Dias, D. K. Singh, S. M. Tommasini, A. H. Haims, M. M. Bandi, and S. Mandre, "Stiffness of the human foot and evolution of the transverse arch," *Nature*, vol. 579, no. 7797, pp. 97–100, 2020.

[9] K. A. Seffen and S. V. Stott, "Surface texturing through cylinder buckling," *Journal of Applied Mechanics, Transactions ASME*, vol. 81, no. 6, pp. 1–7, 2014.

[10] M. Meyer, M. Desbrun, P. Schröder, and A. H. Barr, "Discrete Differential-Geometry Operators for Triangulated 2-Manifolds," pp. 35–57, 2003.

[11] G. Taubin, "Curve and surface smoothing without shrinkage," 1995.

[12] D. Cunto, "Numerical simulation of the post buckling of a constrained thin shell tube," pp. 1–5, 2020.

[13] https://www.thespacereview.com/article/1326/1

[14] Donnell, L. H. and Wan, C. C., "Effects of Imperfections on Buckling of Thin Cylinders and Columns under Axial Compression," *Journal of Applied Mechanics*, Vol. 17, 1950, pp. 73-83.

[15] Koiter, W. T., "Over de Stabiliteit van het Elastisch Evenwicht," University of Delft thesis, Paris, Amsterdam, 1945 (English translation, NASA Rept. TTF-10, 1967).

[16] Ker, R. F., Bennett, M. B., Bibby, S. R., Kester, R. C. Alexander, R. M. "The spring in the arch of the human foot," *Nature* **325**, 147–149 (1987).

[17] Koiter, W. T. "On the nonlinear theory of thin elastic shells. i, ii, iii," *Proceedings of the Koninklijke Nederlandse Akademie van Wetenschappen, Series B* **69**, 1–54 (1966).

[18] Koiter, W. T. "On the foundations of the linear theory of thin elastic shells," *Proceedings of the Koninklijke Nederlandse Akademie van Wetenschappen, Series B* **73**, 169 (1970).

[19] Fluegge, S. *Stresses in shells* (Berlin: Springer, 2nd ed., 1973).

[20] Niordson, F. I. *Shell theory* (Elsevier, 1985).

[21] Horton, W. H., and Durham, S. C., 1965, "Imperfections, A Main Contributor

to Scatter in Experimental Values of Buckling Load," *Int. J. Solids and Struct.*, 1, pp. 59–72.

[22] Ch. 7 Stability of composite shell–type structures, in *Stability and Vibrations of Thin Walled Composite Structures*, edited by H. Abramovich (Woodhead Publishing, 2017) pp. 253 – 428.

[23] Alireza Dastan (2020). Gaussian and mean curvatures calculation on a triangulated 3d surface (https://www.mathworks.com/matlabcentral/fileexchange/61136-gaussian-and-mean-curvatures-calculation-on-a-triangulated-3d-surface), MATLAB Central File Exchange.